



HAL
open science

Virtual synchronous generators for voltage synchronization of a hybrid PV-diesel power system

Ahmed Belila, Yassine Amirat, Mohamed Benbouzid, El Madjid Berkouk, Gang Yao

► **To cite this version:**

Ahmed Belila, Yassine Amirat, Mohamed Benbouzid, El Madjid Berkouk, Gang Yao. Virtual synchronous generators for voltage synchronization of a hybrid PV-diesel power system. International Journal of Electrical Power & Energy Systems, 2020, 117, pp.105677. 10.1016/j.ijepes.2019.105677 . hal-02969932

HAL Id: hal-02969932

<https://hal.science/hal-02969932>

Submitted on 21 Jul 2022

HAL is a multi-disciplinary open access archive for the deposit and dissemination of scientific research documents, whether they are published or not. The documents may come from teaching and research institutions in France or abroad, or from public or private research centers.

L'archive ouverte pluridisciplinaire **HAL**, est destinée au dépôt et à la diffusion de documents scientifiques de niveau recherche, publiés ou non, émanant des établissements d'enseignement et de recherche français ou étrangers, des laboratoires publics ou privés.



Distributed under a Creative Commons Attribution - NonCommercial 4.0 International License

Virtual Synchronous Generators for Voltage Synchronization of a Hybrid PV-Diesel Power System

Ahmed Belila^{a,c}, Yassine Amirat^b, Mohamed Benbouzid^{c,e}, El Madjid Berkouk^d, Gang Yao^e

^a*Ecole Militaire Polytechnique, UER ELT, 16111 Algiers, Algeria.*

^b*ISEN Yncra Ouest Brest, UMR CNRS 6026 IRDL, 29200 Brest, France.*

^c*University of Brest, UMR CNRS 6026 IRDL, 29238 Brest, France*

^d*Ecole Nationale Polytechnique, LCP-lab, 16000 Algiers, Algeria.*

^e*Shanghai Maritime University, Shanghai, China.*

Abstract

To ensure the synchronization process in a hybrid PV-Diesel generation system parallel topology, a phase-locked loop is generally used to estimate the angular frequency of the point of common coupling. However, the DG rotor inaccessibility imposes its operation mode as a master. This will therefore affect the system overall stability since the phase-locked loop is affected by oscillations, which are predicted by the power-angle curve concept interacting with the DG rotary inertia. In this context, this paper proposes a new control strategy based on virtual synchronous generators for a stand-alone PV-Diesel hybrid generation system to synchronize the output voltages without a phase-locked loop, while correcting the diesel generator rotor initial position and ensuring power sharing between the two sources, according to a desired power ratio. To prove the effectiveness of the proposed control strategy, simulation and experiments are carried out. The achieved results clearly illustrated the feasibility and the improvement brought by the proposed virtual synchronous generators-based control strategy.

Keywords: Hybrid generation system, virtual synchronous generator, voltage synchronization, power sharing.

*Corresponding author
*mohamed.benbouzid@univ-brest.fr

List of Symbols

| | | |
|----|------------|-------------------------------------|
| | PVG-DG | PV Generator-Diesel Generator |
| | RES | Renewable Energy Sources |
| | VSG | Virtual Synchronous Generators |
| 5 | PLL | Phase-Locked Loop |
| | PCC | Point of Common Coupling |
| | AVR | Automatic Voltage Regulation |
| | VEV | Virtual Excitation Voltage |
| | PI | Proportional Integral |
| 10 | MPPT | Maximum Power Point Tracking |
| | $T_m(T_e)$ | Mechanical (electromagnetic) torque |
| | $P_m(P_e)$ | Mechanical (electromagnetic) power |
| | E_0 | Stator winding emf |
| | ω | Electrical angular speed |
| 15 | ω_N | Rated electrical angular speed |
| | ω_m | Mechanical speed |
| | J | Rotational inertia |
| | θ | Electrical angle |
| | I_{ph} | Photocurrent |
| 20 | I_0 | Diode saturation current |
| | q | Coulomb constant |
| | k | Boltzmann constant |

| | | |
|----|---------|-------------------------|
| | G | Global insulation |
| | SOC | State of Charge |
| 25 | SOC_0 | Initial State of Charge |

1. Introduction

Various hybrid power generation systems based on diesel generators have been used widely in several applications. The integration of renewable energy sources (RES) such as PV and wind into this type of hybrid energy system have
 30 been a focal point, while the synchronization process of these hybrid systems, connected to the main utility grid through Voltage Source Inverter (VSI), has been indexed as one of the major stability issue.

To ensure the synchronization process a phase-locked loop (PLL) is generally used to estimate the angular frequency of the point of common coupling (PCC).
 35 However, the DG rotor inaccessibility imposes a slave operation mode of the VSI and a master operation mode of the DG as illustrated by Fig. 1.

Since a stand-alone microgrid with a small system inertia is vulnerable to the output power fluctuations of intermittent renewable generation systems [1], the DG master operation mode entails the following drawbacks:

- 40 • The PLL stability is affected by the DG transients [2].
- Oscillations appearance during the sources synchronization. These oscillations are predicted from the power-angle curve concept interacting with the DG rotary inertia. This will therefore affect the overall system stability [3].

45 In this context, this paper proposes a new control strategy based on Virtual Synchronous Generators (VSG) for a hybrid PVG-DG power system in a stand-alone context. This control concept consists in emulating the VSI operation by a synchronous machine. This makes it possible to ensure synchronization at PCC without using a PLL [4] and limits the above-mentioned drawbacks [5].

50 In the literature, the VSG concept was proposed and studied by many re-
searchers quite recently [6]. Main research works were mainly focused towards
its application and the stability analysis [7], [8], [9]. The VSG concept has
been well investigated with different practical implementations [10], [11], [12].
Majority of the carried out investigations were focused on the implementation of
55 the VSG concept for parallel VSIs in microgrids and dealing with the transition
between grid-connected to islanded modes [7], [13], [14]. In [7], an enhanced
VSG control without PLL was proposed for multiple parallel inverters and an
accurate small-signal model of the multiple parallel VSGs system was derived for
system analysis and parameter design. In the same context, a very interesting
60 review of active and reactive power sharing strategies in hierarchical controlled
microgrids has been presented in [15] and an active and reactive power sharing
control strategy for VSGs in microgrid in [16]. In [17], an enhanced VSG control
is proposed, where oscillations damping and proper transient active power shar-
ing are achieved by adjusting the virtual stator reactance based on a state-space
65 analysis. In [13], it is proposed a power decoupling method based on a decou-
pling matrix in the VSG control unit. This method is based on the linearized
power transfer model. In [18], it was proposed an improved dual droop control
(for the VSI and the DC side energy storages) to ensure the VSG functions and
to achieve power management.

70 To achieve higher stability in a microgrid including a small DG, a master
operating mode is required for the VSI. However and as it was previously dis-
cussed, the access to the DG rotor and its initial position, present a challenging
task to impose a slave mode for the DG. To address this issue, this paper pro-
poses a new control strategy based on VSG for a hybrid PVG-DG power system
75 including an Energy Storage System (ESS) in a stand-alone context, to synchro-
nize the output voltages without a PLL, while correcting the diesel generator
rotor initial position and also the ensuring power sharing between the two power
sources according to a desired power ratio. It should be mentioned here that
the stability issue is not addressed in this paper as the considered micro grid is
80 not subject to disturbances inducing high oscillations [19], [20].

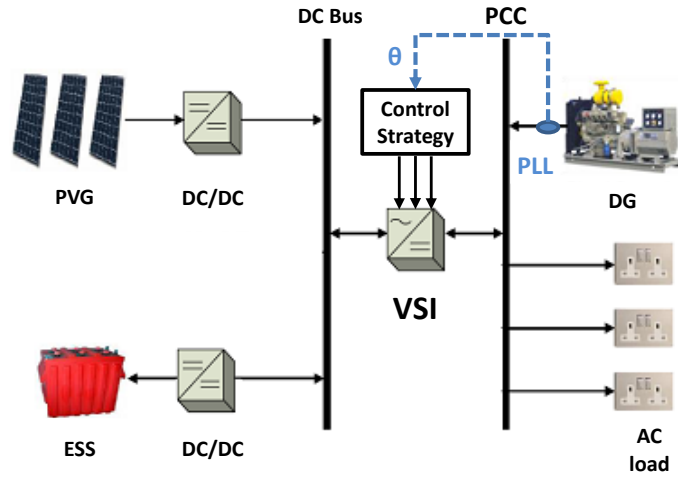


Figure 1: Conventional synchronization process with PLL

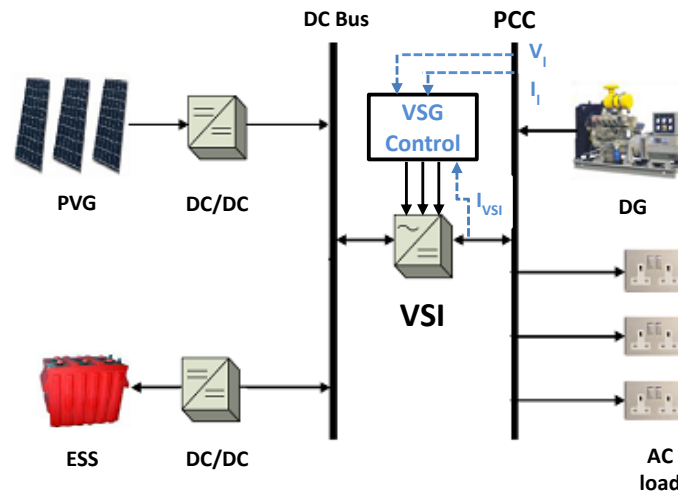


Figure 2: Proposed synchronization Process without PLL

The paper is organized as follows: The system structure and modeling is described in Section 2. In Section 3, the principle of the proposed synchronization method and power sharing control is presented. Simulation results are presented in Section 4, while the experimental ones are given in Section 5. Section 6 concludes the paper.

2. System Structure and Modeling

Figure 2, shows the structure of the parallel hybrid PVG-DG power system using VSG control. The PVG is connected to the DC bus through a boost converter controlled by an MPPT Perturb and Observ (P&O) strategy. The DG is connected to the AC bus and the energy storage system (ESS) is designed for regulating the DC bus voltage in order to supply or absorb insufficient/surplus power generated by PVG and/or DG. The AC bus of the studied system, can be simplified as described in Fig. 3. It consists in connecting in parallel two synchronous generators, a real synchronous generator (RSG), which represents the (DG), and a virtual synchronous generator (VSG)(DG), which represents the VSI associated to the PVG, and ESS sources.

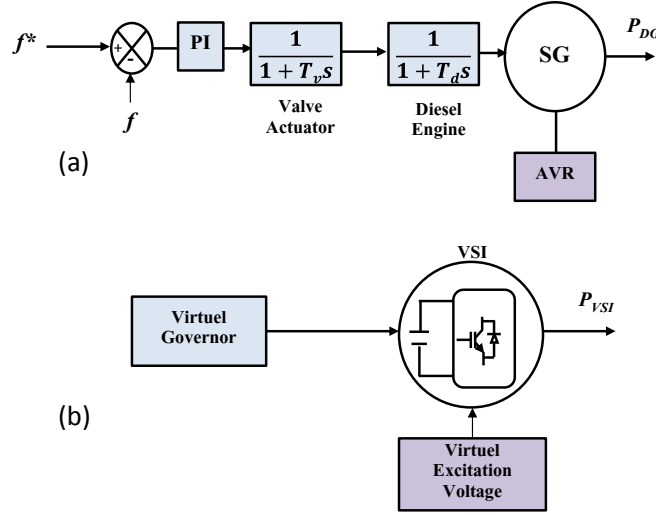


Figure 3: (a) DG block diagram, (b) VSI block diagram.

2.1. Real Synchronous Generator Model

In Fig. 3a, the DG model is illustrated in a block diagram form. This model is widely used and well-describes the dynamic behavior of small DG sets [21]. The valve actuator and the diesel engine are represented by first-order lags, with time constants T_v and T_d , respectively. In this model, the mechanical input of

the synchronous generator is the PI controller output. The relationship between the electromagnetic torque T_m and the angular velocity ω_m of the DG rotor can be expressed by Eq. (1), where J is the combined moment of inertia of the diesel engine and the synchronous generator.

$$J \frac{d\omega_m}{dt} = T_m - T_e \quad (1)$$

It can be noted from Eq. (1) that the system frequency depends on the DG rotational speed and its variation is inversely proportional to the system inertia J . This highlights the fact that DGs with small inertias are vulnerable to load changes as discussed in the Introduction Section [22].

The nominal output voltages of SG are maintained constant by an Automatic Voltage Regulation (AVR) system [21]. The SG and AVR models are referred in the mathworks toolbox user guide.

2.2. Virtual Synchronous Generator Model

According to the VSG principle, the PVG and the ESS can be equivalent to a prime mover (Fig. 3), and the classical three-phase voltage-source inverter VSI will operate as a synchronous generator. In this case, the relevant control strategies and theoretical analysis of a real synchronous generator can be effectively transferred into the studied microgrid [23].

Similarly, the second-order model is a typical one for a VSI [24], [25]. As shown in Fig. 3b, to emulate the DG diesel engine and the AVR system, a virtual governor and a virtual excitation system are respectively used. The mechanical and the electrical parts of VSI are described by the following equations system [5], [10], [12]:

$$\begin{cases} T_m - T_e - D\Delta\omega = \frac{P_m}{\omega} - \frac{P_e}{\omega} - D\Delta\omega = J \frac{d\omega}{dt} \\ \omega = \frac{d\theta}{dt}, \Delta\omega = \omega - \omega_B \\ E_0 = U_s + I(r_a + jx_s) \end{cases} \quad (2)$$

Where T_m and T_e are the mechanical torque of the synchronous generator rotor shaft input from a prime mover and the stator electromagnetic torque,

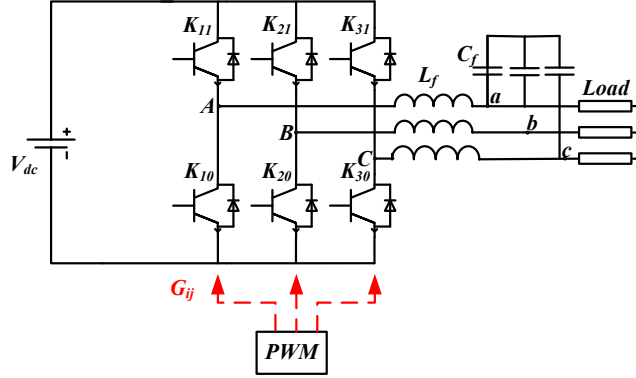


Figure 4: VSI topology.

respectively; D is the damping coefficient used to represent the prime mover damping characteristics; ω is the actual electrical angular velocity and ω_B is rated one. With the assumption of a pole pairs number of 1, mechanical angular velocity $\omega_m = \omega$; P_m and P_e are the mechanical power and electromagnetic power, respectively; J and θ are the rotational inertia and electrical angle, respectively; E_0 is the three-phase stator winding *emf*; U_S and I are the stator voltage and current, respectively, and r_a and x_s are respectively the armature resistance and synchronous reactance.

2.2.1. VSI Model

The schematic diagram of a three-phase voltage source inverter VSI is shown in Fig. 4. It comprises a voltage source at its input and a current source at its output. The connection between these two sources is periodically done through bidirectional current switches.

Assuming that F_{ij} represents the connection function for each switch (K_{ij}):

$$\begin{cases} F_{ij} = 1 \rightarrow if : K_{i1} = 1 \\ F_{ij} = 0 \rightarrow if : K_{i1} = 0 \end{cases} \quad (3)$$

140 Thus, the output voltages of VSI, can be expressed in the following matrix form:

$$\begin{bmatrix} V_{an} \\ V_{bn} \\ V_{cn} \end{bmatrix} = \frac{1}{3}V_{dc} \begin{bmatrix} 2 & -1 & -1 \\ -1 & 2 & -1 \\ -1 & -1 & 2 \end{bmatrix} \begin{bmatrix} F_{11} \\ F_{21} \\ F_{31} \end{bmatrix} \quad (4)$$

2.2.2. PVG Model

The photovoltaic cell is the main part of a PV system. A single-diode model can be used to simulate silicon photovoltaic cells (Fig. 5(a)). A photovoltaic cell is a nonlinear device, which can be modeled by a current source generating the photo current I_{ph} , a diode, a series-resistance taking into account the internal
145 resistance R_S , and a parallel resistance R_P representing the leakage current [26].

$$I_{cel} = I_{ph} - I_0 \left(e^{\left(\frac{V_{pv} + R_s I}{aV_T} \right)} - 1 \right) - \left(\frac{V_{pv} + R_s I}{R_P} \right) \quad (5)$$

With the thermal potential s given by:

$$V_T = \frac{n_s k T}{q} \quad (6)$$

Where I_{cel} and V_{pv} are the output current and voltage of the PV cell, respectively, I_0 is the reverse saturation current, a is the ideality factor, T is the PV
150 temperature (K) and k is the Boltzmann constant [2].

For a PVG containing n_s and n_p panels in series and in parallel, respectively, the output current I_{PVG} is given by:

$$I_{PVG} = n_p I_{ph} - n_p I_0 \left(e^{\left(\frac{V_{pv} + R_{sG} I}{a n_s V_T} \right)} - 1 \right) - \frac{V_{pv} + R_{sG} I_{pv}}{R_{pG}} \quad (7)$$

Where:

$$\begin{cases} R_{sG} = \frac{n_s R_s}{n_p} \\ R_{sP} = \frac{n_s R_p}{n_p} \end{cases} \quad (8)$$

2.2.3. ESS Model

For energy conversion, a simple modeling approach has been adopted for the
155 batteries of ESS [27]. In this model, the battery equivalent circuit is illustrated

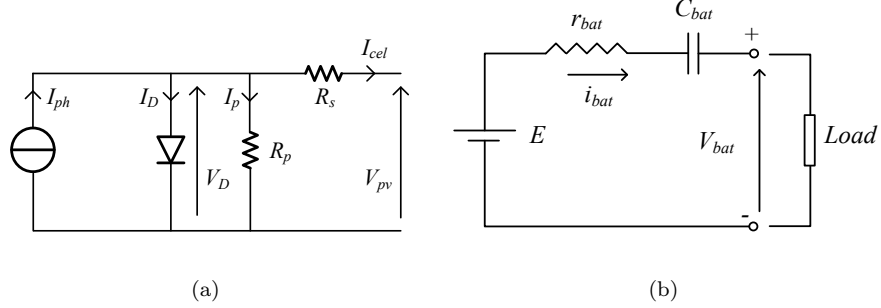


Figure 5: a) PVG model. b) ESS model.

by Fig. 5(b) , where the battery voltage is given by:

$$V_{bat} = E_0 - R_{bat}i - V_{C_{bat}} \quad (9)$$

The battery state of charge (*SOC*) is given by [1],[15][16]:

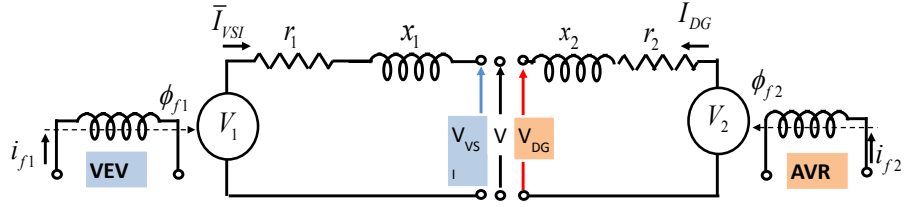
$$SOC(t) = SOC(0) - \frac{1}{C_{bat}} \int_0^t i(t) dt \quad (10)$$

3. Proposed Synchronisation Process and Power Sharing Method

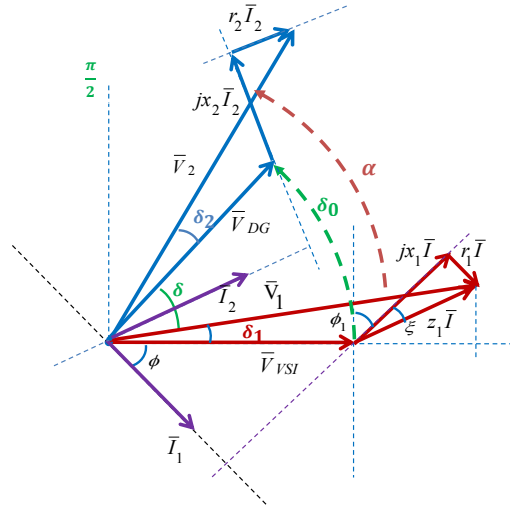
When the VSI and the DG are interconnected, the stator voltages and currents of the real and virtual generators must have the same frequency and the rotor mechanical speed of each is synchronized to this frequency. Therefore, interconnected synchronous generators rotors must be in synchronism.

3.1. Synchronisation Process

Figure 6 shows the equivalent circuit and the phasor diagram of the interconnected synchronous generators before synchronization, where V_{VSI} and V_{DG} represent the VSI and DG output voltage amplitudes, respectively. V_1 and V_2 are the virtual and real electromotive force, respectively; (δ_1, δ_2) are the phase angles difference between (V_1, V_{VSI}) , and (V_2, V_{DG}) , respectively. δ_0 is the phase-shift between V_{VSI} , V_{DG} ; α is the rotor initial phase of the DG; (x_1, r_1)



(a)



(b)

Figure 6: Simplified connection of the two sources before synchronization: a) Equivalent circuit. b) Phasor diagram.

170 are the VSI filter reactance and resistance, respectively; and (x_2, r_2) are the DG
 stator reactance and resistance, respectively.

To ensure the two sources synchronization, the two output voltages V_{VSI}
 and V_{DG} , must be superimposed thus imposing a zero phase-shift $\delta_0 = 0$.

From the phasor diagram in Fig. 6(b), it is clear that under no-load operation,
 175 the synchronism ($\delta_0 = 0$) can be ensured only by the correction of the
 rotor initial position (α). In this mode, the correction of α is determined in
 relation to (x_1, r_1) and (x_2, r_2) , as it will be latter detailed.

The active and reactive powers of the VSI and DG can be written as fol-

lows [16], [28]:

$$\begin{cases} P_{VSI} = \frac{V_1}{(r_1)^2+(x_1)^2}(r_1(V_1 - V_{VSI}\cos\delta_1) + x_1V_{VSI}\sin\delta_1) \\ Q_{VSI} = \frac{V_1}{(r_1)^2+(x_1)^2}(-r_1V_{VSI}\sin\delta_1 + x_1(V_1 - V_{VSI}\cos\delta_1)) \end{cases} \quad (11)$$

$$\begin{cases} P_{DG} = \frac{V_2}{(r_2)^2+(x_2)^2}(r_2(V_2 - V_{DG}\cos\delta_2) + x_2V_{DG}\sin\delta_2) \\ Q_{DG} = \frac{V_2}{(r_2)^2+(x_2)^2}(-r_2V_{DG}\sin\delta_2 + x_2(V_2 - V_{DG}\cos\delta_2)) \end{cases} \quad (12)$$

180 To ensure the two sources synchronization under loaded operation, a zero phase-shift ($\delta_0 = 0$) must be imposed via the correction of the rotor initial position ($\alpha_i \neq 0$), which is determined according to the desired power ratio between the two sources (R_i).

Figure 7 shows the equivalent circuit and the phasor diagram under load 185 operation, of the interconnected synchronous generators after synchronization, where the two output voltages V_{VSI} and V_{DG} are superimposed ($V = V_{VSI}=V_{DG}$).

From Eqs.(11) and (12), the active and reactive powers that the VSI and DG will deliver to the PCC under load operation can be rewritten as follows:

$$\begin{cases} P_{VSI} = \frac{V_1}{(r_1)^2+(x_1)^2}(r_1(V_1 - V\cos\delta_1) + x_1V\sin\delta_1) \\ Q_{VSI} = \frac{V_1}{(r_1)^2+(x_1)^2}(-r_1V\sin\delta_1 + x_1(V_1 - V\cos\delta_1)) \end{cases} \quad (13)$$

$$\begin{cases} P_{DG} = \frac{V_2}{(r_2)^2+(x_2)^2}(r_2(V_2 - V\cos\delta_2) + x_2V\sin\delta_2) \\ Q_{DG} = \frac{V_2}{(r_2)^2+(x_2)^2}(-r_2V\sin\delta_2 + x_2(V_2 - V\cos\delta_2)) \end{cases} \quad (14)$$

Note here that, since the two sources are directly connected to the PCC, the 190 lines impedances r_{L1}, x_{L1} and r_{L2}, x_{L2} after the (PCC) are included in P_{load} and Q_{load} .

In this paper, the P/f and Q/V droop control strategies will be discussed for the considered hybrid PVG-DG-ESS system, under the assumption that the line impedance is approximately inductive. This assumption is based on the fact that the line impedance of the virtual and real stators winding is approximately inductive. Indeed, the resistive part of each stator winding can be neglected compared to the inductive one and the power angles δ_1 and δ_2 in such lines are small. It can then be assumed that: $\sin\delta_1 = \delta_1$, $\sin\delta_2 = \delta_2$

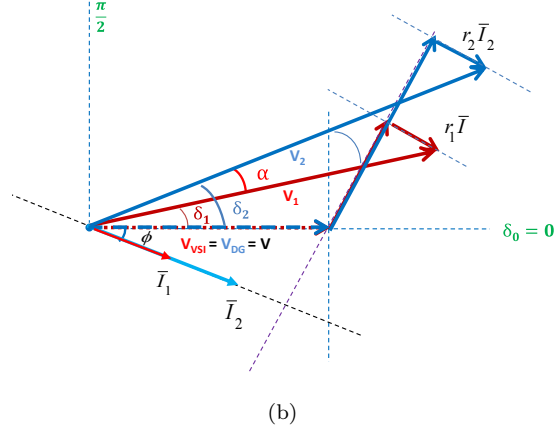
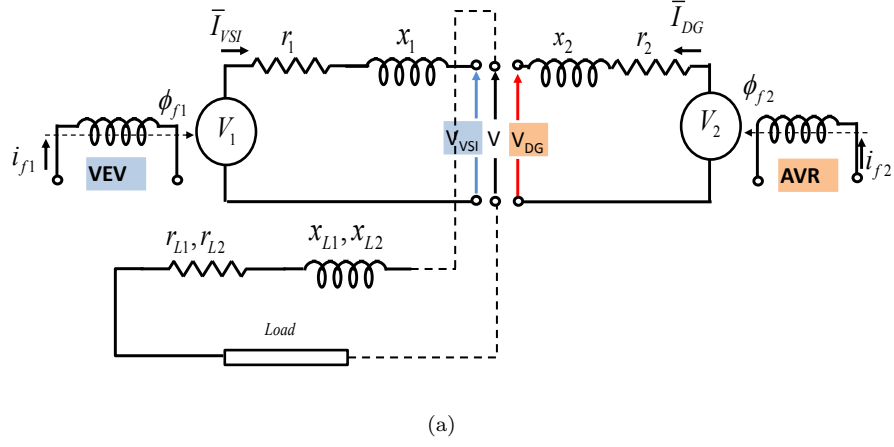


Figure 7: Simplified connection of the two sources after synchronization: a) Equivalent circuit. b) Phasor diagram.

and ($\cos \delta_1 = \cos \delta_2 = 1$). In addition, when the two sources are synchronized at PCC (Fig. 7(b)), we have:

$$\begin{cases} \delta_2 = \delta_1 + \alpha \\ V_{VSI} = V_{DG} = V \end{cases} \quad (15)$$

Therefore allowing rewriting Eqs.(13) and (14) as:

$$\begin{cases} P_{VSI} = \frac{V_1 V \delta_1}{x_1} \\ Q_{VSI} = \frac{V_1 (V_1 - V)}{x_1} \end{cases} \quad (16)$$

$$\begin{cases} P_{DG} = \frac{V_2 V (\delta_1 + \alpha)}{x_2} \\ Q_{DG} = \frac{V_2 (V_2 - V)}{x_2} \end{cases} \quad (17)$$

The following power ratio can therefore be deduced.

$$\begin{cases} R_P = \frac{P_{VSI}}{P_{DG}} = \frac{V_1 x_2}{V_2 x_1} \frac{\delta_1}{\delta_1 + \alpha} \\ R_Q = \frac{Q_{VSI}}{Q_{DG}} = \frac{x_2}{x_1} \frac{V_1}{V_2} \frac{V_1 - V}{V_2 - V} \end{cases} \quad (18)$$

Where, R_P and R_Q are the desired active and reactive power ratios between the two sources, respectively. These relations show that it is possible to ensure the synchronization between the two energy sources by a judicious control of the active and reactive power delivered by the VSI . It particularly highlights a very interesting method to correct the rotor initial position α of the DG, since the exchanged active and reactive powers can be fixed beforehand through the control. Indeed, the initial angle of the DG rotor can be expressed as follows:

$$\alpha = \delta_1 \left(\frac{V_1 x_2}{V_2 x_1} \frac{1}{R_P} - 1 \right) \quad (19)$$

This angle, which can be fixed beforehand mainly according to the VSI power angle δ_1 , the ratio between the reactances of the real and the virtual stator winding $\frac{x_2}{x_1}$, the desired active power ratio R_P and the ratio between the virtual and real electromotive force ($\frac{V_1}{V_2}$) which is corresponding to the desired reactive power ratio R_Q . Indeed, Eq. 19 can be expressed as a function of R_P and R_Q as follows:

$$\alpha = \delta_1 \left(\frac{R_Q}{R_P} \cdot \frac{V_2 - V}{V_1 - V} - 1 \right) \quad (20)$$

This relation gives rise to two distinguished correction of the rotor initial position:

- When the active and reactive power ratios between the two sources are the same $R_P = R_Q$. In this case the desired power ratio is ($R = R_P = R_Q$) and whatever its value, a zero angle of the rotor initial position must be imposed ($\alpha = 0$).

- When the active and reactive power ratios between the two sources are different $R_P \neq R_Q$. In this case, for each value of (R_P, R_Q) , a phase-shift between the two sources must be imposed through the rotor initial position ($\alpha_{pq} \neq 0$).

It is clear from Eq.(20), that unlike the first case, the second case corresponding to $(R_P \neq R_Q)$, requires a prior identification of the value of δ_1 , to impose a rotor initial position ($\alpha_{pq} \neq 0$).

3.2. VSG-based Control Strategy

To properly share the active and reactive powers between the two sources, the desired power ratios R_P and R_Q should be equally designed, as it has been above-discussed. Therefore, the proposed VSG-based control scheme, shown in Fig. 8, can be subdivided on in six control parts: Power calculation, Virtual inertia, Virtual Governor, Virtual excitation system, References voltages generation and DG rotor initial position correction.

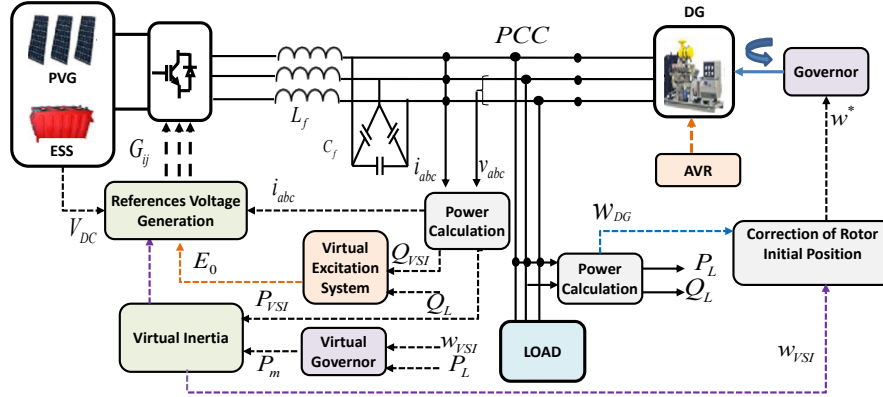


Figure 8: proposed VSG-based control scheme.

3.2.1. Power Calculation

Equations describing the instantaneous active and reactive powers are expressed, according to the output voltages and currents taken from the LC filter

interface measurements, as:

$$\begin{cases} P(t) = v_a i_a + v_b i_b + v_c i_c \\ Q(t) = \frac{1}{\sqrt{3}} [(v_b - v_c) i_a + (v_c - v_a) i_b + (v_a - v_b) i_c] \end{cases} \quad (21)$$

3.2.2. Virtual Inertia

The emulation of a rotating inertia is the main difference between the VSG control strategy and the conventional droop control [29]. The virtual inertia control scheme, shown in part 1 of Fig. 9, is based on a conventional swing equation (Eq.(2)), representing the inertia and damping of a traditional synchronous generator, where the acceleration of the inertia is determined by the power balance between the virtual mechanical input power P_m , the measured electrical power flowing from the VSI output P_{VSI} , and the damping effect which is defined by the damping coefficient D and the difference between the rotor angular frequency w and its rated value w_n .

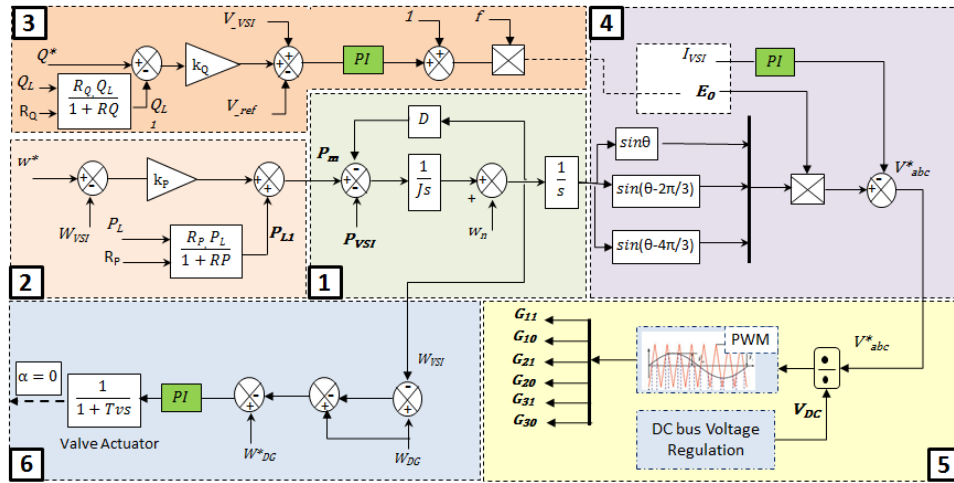


Figure 9: VSG control scheme: (1) Virtual Inertia, (2) Virtual governor system, (3) Virtual excitation voltage, (4,5) Voltage references generation, (6) Correcting the DGrotorinitial position.

240 *3.2.3. Virtual Governor System*

To emulate the DG speed governor characteristics, the traditional frequency droop control is used. As shown in Part 2 of Fig. 9, the virtual mechanical input power P_m of the virtual inertia block is given by the sum of the active load power reference P_{L1} , and the frequency droop effect, where k_p is the frequency adjustment coefficient [30]. The active load power reference P_{L1} can be determined as a function of the active power required by the load P_L and R_P , as follows:

$$P_{L1} = P_L \left(\frac{R_P}{R_P + 1} \right) \quad (22)$$

250 The droop controllers P/f equation is given as follows, where k_p is the frequency adjustment coefficient [31]:

$$P_m - P_{L1} = k_p(\omega^* - \omega_{VSI}) \quad (23)$$

However, and especially for the practical implementation when a low-pass filter (LPF) need to be used to filter the averaged active and reactive output powers, Eq.(23) can be rewritten as follows:

$$P_m - P_{L1} = \left(\frac{m}{\tau p + 1} \right) (\omega^* - \omega_{VSI}) \quad (24)$$

255

Where τ is the time-constant of the low-pass filter and m is the P/w droop coefficient which, can be chosen according to the maximum and minimum values of the allowable angular frequency ($\omega_{max}, \omega_{min}$) and the maximum and minimum capacities of the active power (P_{max}, P_{min}) as follows [32]:

$$m = \frac{\omega_{max} - \omega_{min}}{P_{max} - P_{min}} \quad (25)$$

260

Equation(24) can be rewritten as follows:

$$\frac{\tau}{m} \frac{d}{dt} (\omega_{VSI} - \omega^*) = (P^* - P_{L1}) - \frac{1}{m} (\omega_{VSI} - \omega^*) \quad (26)$$

By comparing Eq.(26) with the classical second-order swing equation (Eq.(2)), the damp term and inertia term D and J are equivalent to:

$$\begin{cases} D = \frac{\tau}{m} = \frac{P_{max} - P_{min}}{\omega_{max} - \omega_{min}} \\ J = \frac{1}{m} \end{cases} \quad (27)$$

265 This relation shows on one hand that the system response is slow with a relatively large inertia and quick with a relatively small inertia and on the other hand that the damping coefficient D , is responsible for the low-frequency fluctuation in steady-state. In the proposed control strategy the damping coefficient D must be adjusted according to the desired power ratio R .

270 3.2.4. Virtual Excitation Voltage

To keep the VSI output voltage amplitude under control, the droop regulation technique is used for the reactive powers exchange with the DG source.

From Eq.(16), the VSI output reactive power that will be delivered to the load can be written as:

$$V_1 - V \approx x_1 \frac{Q_1}{V_1} \quad (28)$$

The voltage amplitude depends then mainly on the reactive power flow. The following droop control expression can be written as:

$$(V_{VSI} - V_0) = -k_Q(Q_{VSI} - Q_0) \quad (29)$$

275

On the other hand, and according to the principle of Synchronous Generator, the excitation electromotive force V_1 can be expressed as:

$$V_1 \approx V + x_{1SR} I_{1q} \quad (30)$$

Where I_{1q} and x_{1SR} are the reactive current and the virtual synchronous reac-
 280 tance, respectively.

Let M_{f1} denotes the mutual inductance amplitude of the virtual stator wind-
 ings, and C denotes the virtual excitation current. Thus the amplitude of the
 virtual excitation electromotive force can be expressed as [12]:

$$V_1 = \omega M_{f1} i_{f1} \quad (31)$$

If we assume that V_{1B} is the base value of V_1 and i_{f1B} is the base value of
 285 i_{f1} (in pu), thus, the virtual excitation voltage and current can be expressed (in
 pu) as follows:

$$\begin{cases} V_{1*} = \frac{V_1}{V_{1B}} = \frac{\omega M_{f1} i_{f1}}{\omega M_{f1} i_{f1B}} = \omega_* i_{f1*} \\ i_{f1*} = \frac{i_{f1}}{i_{f1B}} = \frac{i_{f1B} + \Delta i_f}{i_{f1B}} = 1 + \Delta i_{f1*} \end{cases} \quad (32)$$

With the VEV, when it changes, the terminal voltage V_1 changes with a very
 small slope k , and unlike the AVR, the characteristic $V_1 = f(i_{f1})$ is linear (no
 290 magnetic saturation). The slope K denotes a voltage adjustment coefficient,
 which is defined as follows:

$$K = \frac{V_0 - V_1}{V_N} \quad (33)$$

Where V_0 and V_1 are the VSI terminal voltages without and with load, respec-
 tively and V_N is its rated voltage. Thus, the VEV block diagram is given in
 Part 3 of Fig. 9. The adopted approach for the calculation of its parameters
 295 can be found in [12].

3.2.5. References Voltages Generation

As shown in Part 4 of Fig. 9, the reference voltages V_{abc}^* are reconstructed
 by combining the amplitude information E_0 generated by the virtual excitation
 voltage and the phase information θ generated by the virtual inertia as:

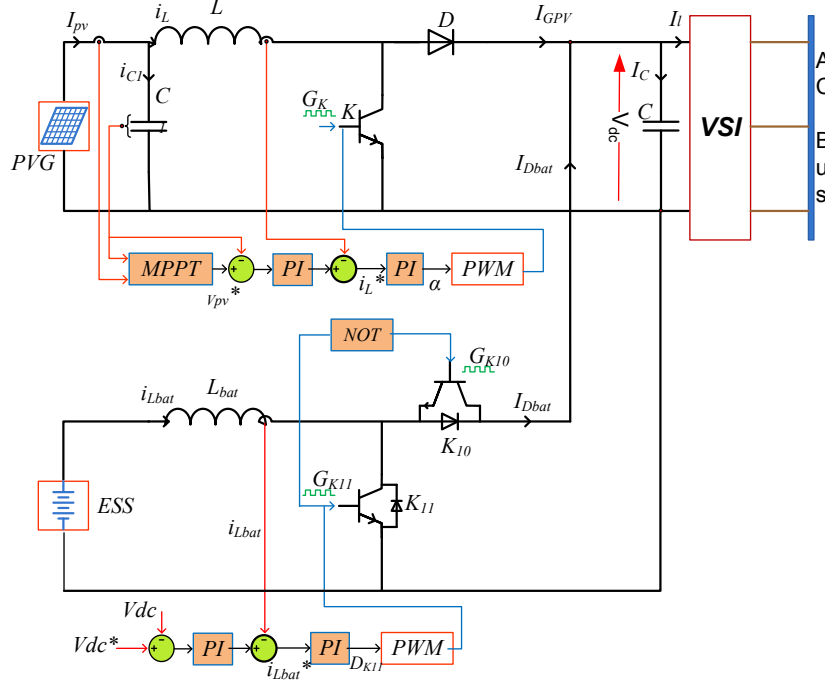


Figure 10: V_{dc} voltage regulation .

$$\begin{cases} V_a^* = \sqrt{2}E_0 \sin\theta \\ V_b^* = \sqrt{2}E_0 \sin(\theta - \frac{2\pi}{3}) \\ V_c^* = \sqrt{2}E_0 \sin(\theta - \frac{4\pi}{3}) \end{cases} \quad (34)$$

300 The voltage references thus obtained are divided by the regulated DC bus voltage V_{dc} to generate in the PWM modulation index m , as shown in Part 5 of Fig. 9. As shown by Fig. 10, the ESS is designed to regulate V_{dc} , in order to supply or absorb insufficient or surplus powers. Indeed, the DC bus voltage can be expressed by:

$$C \frac{d}{dt} (V_{dc}) = i_{PVG} + i_{Dbat} - i_L \quad (35)$$

305 *3.2.6. DG Rotor Initial Position Correction.*

As previously discussed, to ensure the same power sharing between the two sources, it is sufficient to impose a zero-angle of the rotor initial position ($\alpha = 0$).

As shown in Part 6 of Fig. 9. This correction can be achieved through an acceleration or deceleration to the DG rotor according to its initial position.

310 *3.3. Problems of Reactive Power Sharing in Hybrid system (PVG-DG)*

As discussed in the Introduction Section, the rotor accessibility problem of the DG, influences not only the synchronization process, but also the reactive energy and therefore its sharing with other sources due to the limitation of the AVR. In fact, to regulate the DG output voltage, the AVR maintains the
 315 constant voltage up to a certain level by controlling its field winding.

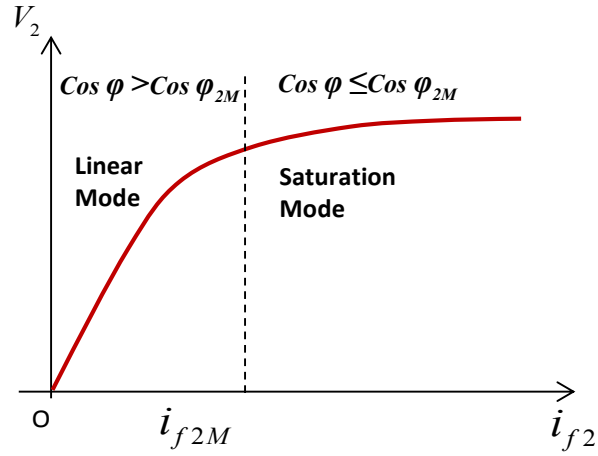


Figure 11: Excitation electromotive force characteristic.

The winding of the rotor field is excited by a direct current i_f . It is through the generated magnetic flux that the AVR compensates the voltage droop or the overvoltage according to the nature of the fed load (inductive or capacitive). Nevertheless this compensation is limited by saturating the magnetic material as
 320 shown in Fig. 11. This justifies the $\cos \phi_{2M}$ often marked on the DG nameplate, defined as:

$$\cos \phi_{2M} = \frac{P_{DG}}{S_{DG}} = \frac{P_2}{S_2} \quad (36)$$

Beyond this value of $\cos \phi_{2M}$, the AVR system is no longer able to maintain the output voltage in term of amplitude.

Due to this limitation of the AVR system, the reactive load sharing cannot
 325 fully satisfy Eq.(18).

From a control theory point of view, the design equation of the AVR system is based on the rotor winding geometrical and material parameters. The maximal excitation current i_{fM} , which also corresponds to the maximal flux ϕ_{f2M} and to the maximal excitation voltage V_{f2M} , could be expressed as [33]:

$$i_{f2M} = \frac{k_w a_w}{\rho L_m} \phi_{fM}^2 R_{fM} \frac{1}{v_{f2M}} \quad (37)$$

330 The geometric, electric, and magnetic parameters of the core and winding window are: the winding window utilization factor K_w ; the winding window area a_w ; the cooper resistivity ρ ; the mean length per turn L_m , and the magnetic reluctance R_{fM} . All these parameters could be replaced with a global core parameter K_n [33]. Eq.(37) can be written as:

$$i_{f2M} = \frac{k_n}{v_{f2M}} \quad (38)$$

335 The electromotive force V_2 is directly proportional to the reactive component of the excitation current i_f , the actual electrical angular velocity, and the mutual inductance of the stator windings M_f [12].

$$V_2 = \omega M_f i_f \quad (39)$$

Its maximum value is therefore:

$$V_{2M} = \omega M_f i_{f2M} \quad (40)$$

Since there is no saturation in virtual excitation voltage (VEV), the limita-
 340 tion of the AVR system can be compensated by the VEV.

According to the load $\cos \phi$, two possible cases can be distinguished.

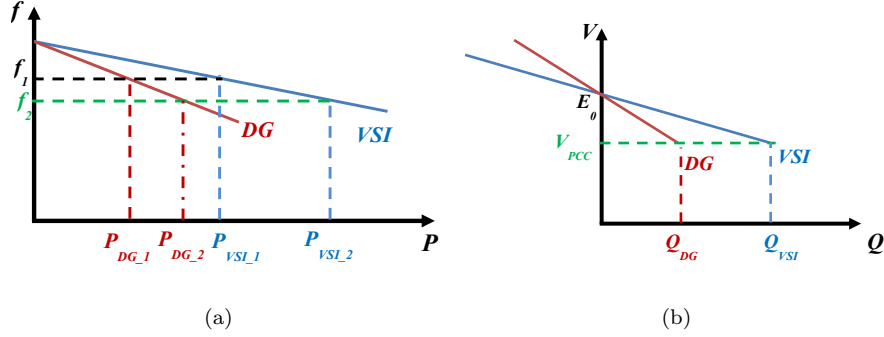


Figure 12: Droop controls for $R = 2$. a) f/P droop control , b) V/Q droop control .

- Case 1: When the load $\cos \phi$ is greater than the DG one ($\cos \phi \geq \cos \phi_{2M}$). Following the proposed control strategy described in Section.3, the active and reactive powers sharing can be achieved according to the desired power ratio ($R = R_P = R_Q$), by imposing a rotor initial position zero-angle ($\alpha = 0$).

Fig. 12(a) and Fig. 12(b) show the principles of f/P and V/Q droop controls, respectively, for a desired power ratio ($R = 2$). Based on this predefined linear droop characteristic, for a desired active powers sharing ratio ($R_P = 2$), $\omega_{m1} = \omega_{m2}$ can be guaranteed in steady-state. In the same way, to share the reactive power according to the desired reactive powers sharing ratio ($R_Q = 2$), an equal output voltage $V = V_{VSI} = V_{DG}$ is required.

- Case 2: When the load $\cos \phi$ is lower than the DG one ($\cos \phi < \cos \phi_{2M}$). The reactive power of the DG must be lower than that of the VSI in order to maintain the above-cited $\cos \phi$ condition, whatever the reactive power required by the load.

Figure 13 show the principle of V/Q droop control when $\cos \phi < \cos \phi_{2M}$. In this case, the desired power ratio R must be imposed according to Q_{2M} , in order to prevent the AVR operation in its saturation area. It can therefore be

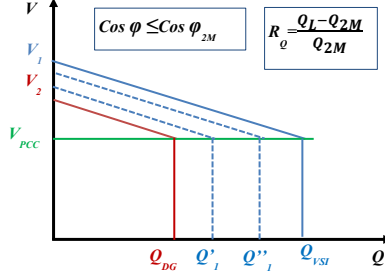


Figure 13: V/Q droop controls for $\cos \varphi \leq \cos \varphi_{2M}$

expressed as follows:

$$R = R_P = R_Q = \frac{Q_1}{Q_{2M}} = \frac{Q_L}{Q_{2M}} - 1 \quad (41)$$

4. Simulation Results

In this section, the effectiveness of the proposed VSG-based control strategy, is evaluated by simulating the hybrid power system described in Fig. 2 with the parameters given in Table 1.

The functional behavior of the system energy sources as well as the synchronization process between the VSI and the DG are illustrated in this section by means of numerical simulation of a few relevant cases. The electrical load comprises both resistive and inductive components that are connected in parallel to the AC bus as shown in Fig. 2. Based on the proposed control strategy, the desired power ratio is fixed to $R = R_P = R_Q = 2$. In this case, the synchronization between the VSI and the DG is guaranteed since $(\omega_1 = \omega_2 = \omega)$ and $(V_1 = V_2 = V)$ in steady-state, as described by Fig.12(a) and Fig.12(b).

The simulation is divided into several time intervals to evaluate the dynamic performance of the VSI, DG, PVG, and ESS under loading transitions. Initially, the system operates with load1, then load2 is connected at $t = 1s$ before cutting-off from the system at $t = 2s$.

The active and reactive powers dynamic responses are shown in Fig. 14(a) and Fig. 14(b), respectively. It is clear that during the three simulation steps

Table 1: Simulation parameters.

| PVG Parameters | | DG Parameters | |
|----------------|--------|----------------|----------|
| PVG RP | 3.2 kW | DG RP | 10 KVA |
| Panel RP | 135 W | τ_1 | 0.03 sec |
| ns | 9 | τ_2 | 0.05 sec |
| np | 4 | ka | 2.7 |
| T | 25 ° | r_2 | 0.6Ω |
| a | 1.3 | x_2 | 5mH |
| ESS Parameters | | VSI Parameters | |
| V_{bat} | 12 V | r_1 | 0.6Ω |
| C_{bat} | 150 Ah | x_1 | 5mH |
| r_{bat} | 1 Ω | C_f | 0.033mF |
| L_{bat} | 0.05 H | L_f | 0.048 mH |

380 ($0 < t < 1s$, $1 < t < 2s$, and $2 < t < 3s$), the two sources (VSI and DG), share respectively ratio of 2/3 and 1/3 of the active and reactive powers requested by the load. The desired active and reactive power sharing between the two sources is obtained because the ratios are the same, as discussed in Section 3. In this case, $P_{VSI} = 2P_{DG} = 2/3P_{load}$ and $Q_{VSI} = 2Q_{DG} = 2/3Q_{load}$. It can also be
385 observed that a transient regime appears at the beginning of the two sources synchronization. This transient regime is due to the DG required time to correct its initial position by imposing $\alpha = 0$, as explained in Subsection 3.2.6.

Figure 15(a) illustrate the output voltages at PCC. It can be observed that the AC voltage is not influenced by the load changes. Both AVR and VEV
390 systems compensate the voltage drop due to the reactive power of each source ($Q_{VSI} = 2Q_{DG} = 2/3Q_{load}$). Moreover, the DG rotor initial position correction can be clearly observed in the zoom of the AC voltage depicted by Fig. 15(b).

Figures 16(a) and 16(b) show the battery currents and the PVG output power, respectively. It can be noticed that when the load current is higher than
395 the PVG one, the ESS is therefore in the discharging state ($I_{bat} > 0$) and when

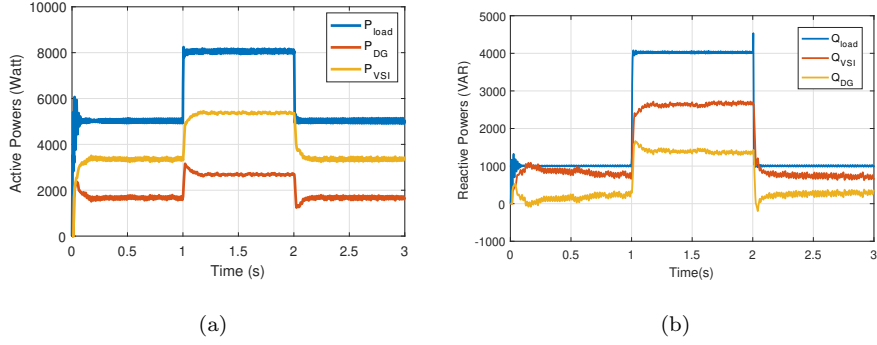


Figure 14: Powers sharing simulation results. a) Active power, b) Reactive power.

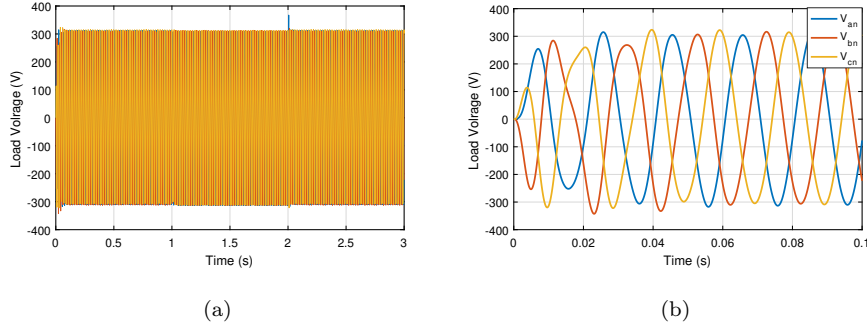


Figure 15: Simulation results in AC bus. a) Output voltages at PCC, b) Zoom of output voltages.

the load current increases, the ESS moves to the charging state ($I_{bat} < 0$).

The frequency dynamic performance at PCC during the loading transition is illustrated by Fig. 17(a). It can be observed that the DG frequency deviations are compensated by the VSI frequency ones, in order to keep a constant frequency, which means that the VSI provides a virtual inertia to the system to allow a better stability.

Figure 17(b) is provided to highlight the DC bus voltage regulation by an ESS through a buck-boost converter as described in Fig. 10. It can be noticed that the DC bus voltage is not affected by the load variation and it is well regulated at 650V, therefore proving the performance of the proposed control.

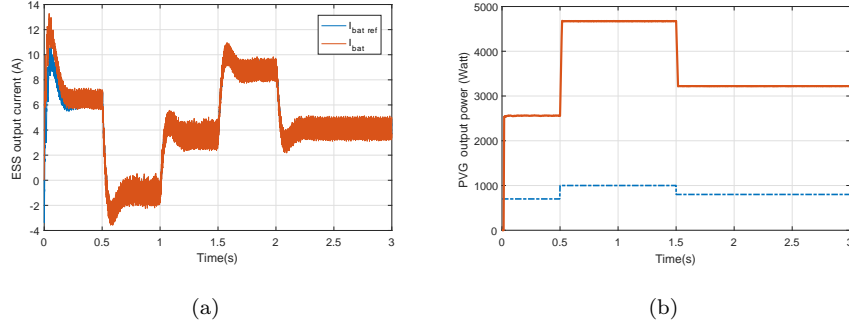


Figure 16: simulation results in DC bus. a) ESS output current, b) PVG output Power.

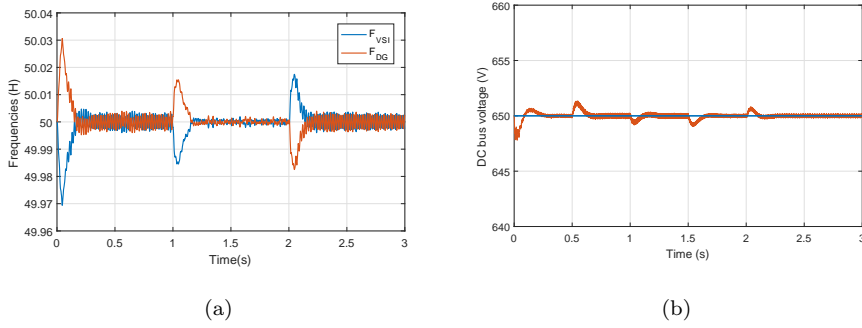


Figure 17: a) Frequency at PCC, b) DC bus voltage.

5. Experimental Results

Real-time experiments are carried out using the **PCI 6281 card controller board with input/output interface**. Figure 18 shows the developed experimental test bench and its main components. The synchronization process and power sharing method control blocks are implemented on a reduced-scal test bench, to show the practical feasibility of the proposed VSG-based control strategy. However, it should be mentioned that due to DG unavailability and difficulty for indoor use, a second VSI is used for emulation purposes. Its virtual mechanical parameters correspond to those of a DG with a rated power of 10 kVA.

Experimental tests were carried out for two cases. In the first case, the second

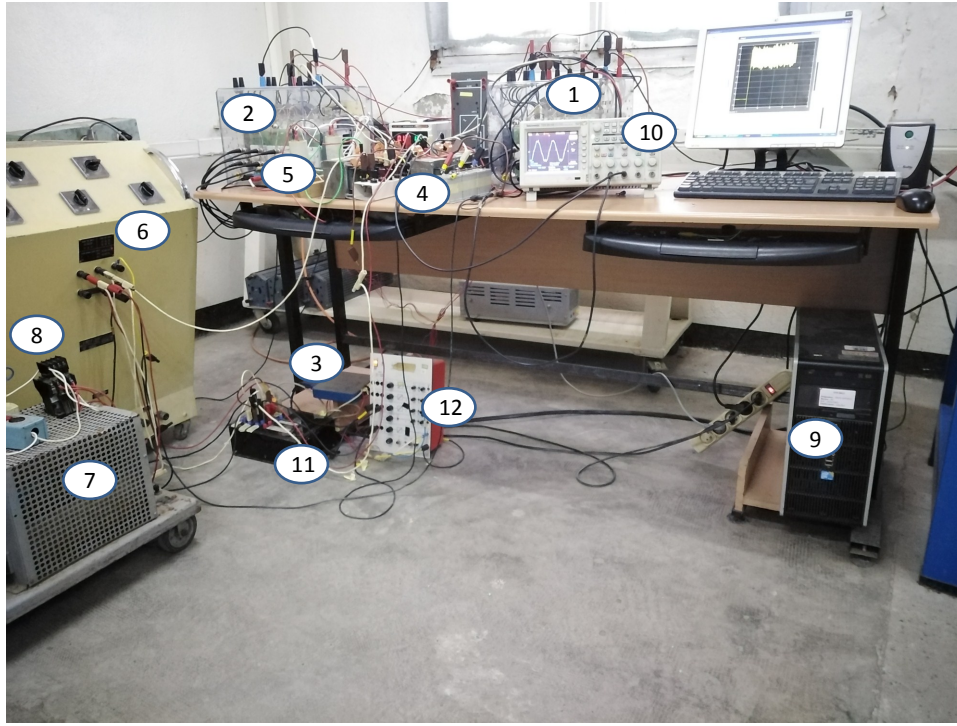


Figure 18: Experimental test bench. (1) VSI1, (2) VSI2, (3) PCI 6281 card controller board with input/output interface, (4) LC filter 1, (5) LC filter 2, (6) Resistive load, (7) Inductive load, (8) load switch, (9) PC, (10) Scope, (11) Current measurement, (12) Voltage measurement.

VSI is connected during a very precise time interval in order to illustrate the synchronization process, while in the second case the two VSIs are connected in parallel in order to evaluate the practical feasibility of the power sharing between the two power sources according to the desired power ratio R .

420 5.1. Synchronization Process Experimental Validation

In order to illustrate the synchronization process between the two voltage source inverters VSI_1 and VSI_2 , the load power is initially provided by VSI_1 , after that, the VSI_2 is connected at $t = 5s$ before cutting off from the system at $t = 25s$.

425 The test has been carried out for a purely resistive load with a desired power

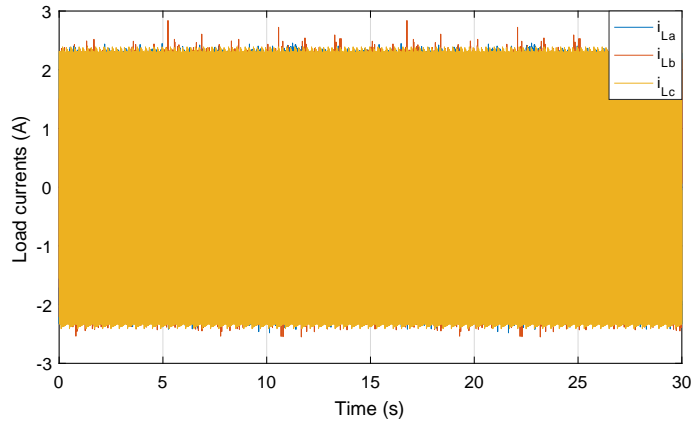


Figure 19: Load currents.

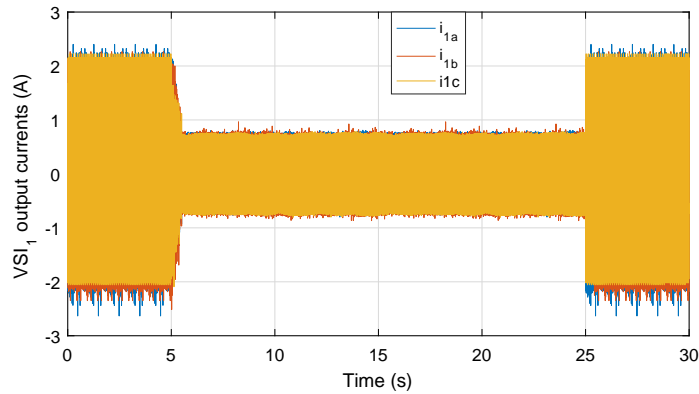


Figure 20: VSI1 output currents.

ratio $R = P_1/P_2 = P_1/P_2 = 1/2$. At the instant of connection of the second inverter VSI_2 , the output voltages V_1 and V_2 are not superimposed.

As discussed in Subsection 3.2.6, the correction of the initial position can be achieved through an acceleration/deceleration of the virtual DG rotor. The synchronization can be ensured by the correction of the VSI_2 virtual rotor initial position by imposing a zero-angle ($\alpha = 0$) through the reconstruction of the

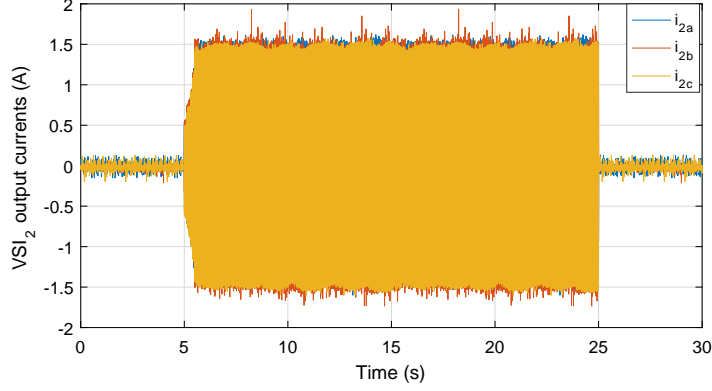


Figure 21: VSI2 output currents.

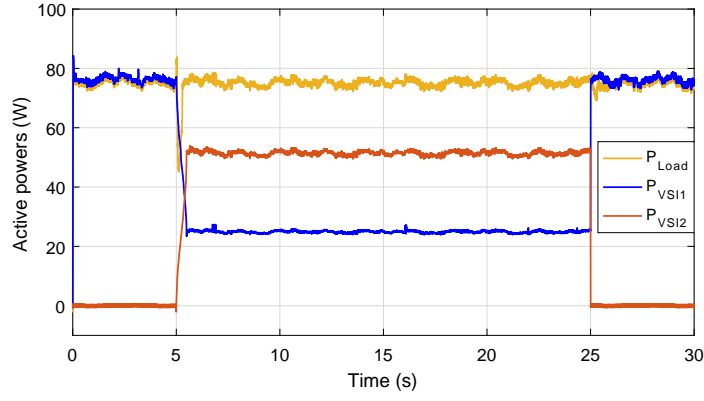


Figure 22: Active power sharing.

reference voltages as follows:

$$\begin{cases} V_{a2}^* = \sqrt{2}E_{02}\sin(\theta - \alpha) \\ V_{b2}^* = \sqrt{2}E_{02}\sin(\theta - \frac{2\pi}{3} - \alpha) \\ V_{c2}^* = \sqrt{2}E_{02}\sin(\theta - \frac{4\pi}{3} - \alpha) \end{cases} \quad (42)$$

From the experimental results depicted in Figs. 19 to 21, it can be clearly seen that after the second VSI connection, the load power is shared between the two VSIs, according to the desired power ratio $R = 1/2$. In fact, the first provides $1/3P_{load}$ while the second provides $2/3P_{load}$. The microgrid consists in this case of two grid-forming power converters connected in parallel and con-

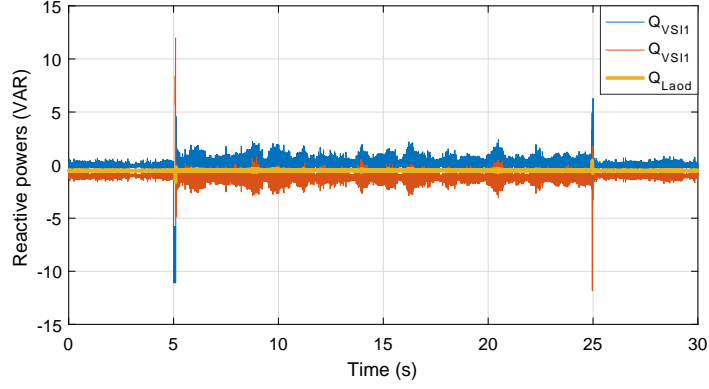


Figure 23: Reactive power sharing.

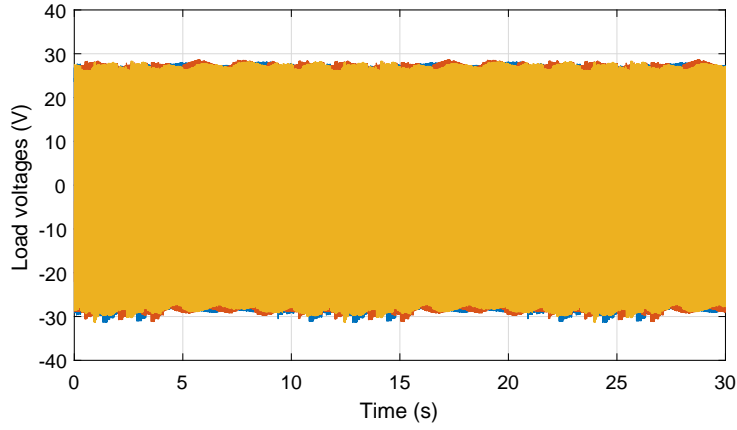


Figure 24: Output voltages in AC bus.

trolled in closed-loop to work as ideal AC voltage sources with a given amplitude $V_{max} = 28V$ and frequency $f = 50Hz$. As voltage sources, they present a low-output impedance. The currents flowing through their output impedances are expressed as:

$$I_{VSI2} = 2I_{VSI1} = \frac{2}{3}I_{Load} \quad (43)$$

The virtual excitation voltage (V_{f2}) of VSI₂ must be greater than V_{f1} in order to compensate the voltage drop (see Subsection.3.2.4). The virtual electromotive

Table 2: Experimental validation parameters.

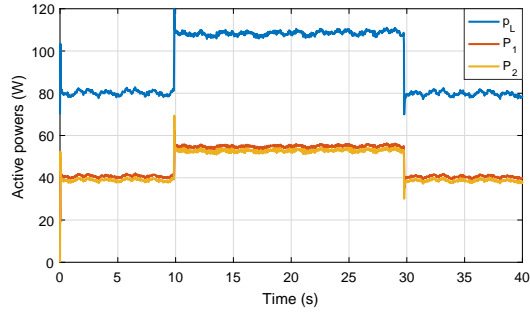
| VSI ₁ Parameters | | VSI ₂ Parameters | |
|-----------------------------|---------------------|-----------------------------|--------------|
| Parameter | Value | Parameter | Value |
| r_1 | 3.8Ω | r_2 | 3.8Ω |
| x_{R1}, x_{R2}, x_{R3} | $10, 20, 26mH$ | x_2 | $10mH$ |
| $cf_{R1}, cf_{R2}, cf_{R3}$ | $50, 100, 330\mu F$ | c_f | $30\mu F$ |
| J_1 | $0.22kg.m^2$ | J_2 | $0.06kg.m^2$ |
| D_{R1}, D_{R2}, D_{R3} | $2, 4, 6$ | D_2 | 2 |
| K_{Q1} | 0.0001 | K_{Q2} | 0.0001 |
| K_{p1} | 1000 | K_{p2} | 2000 |

forces are not the same ($V_1 > V_2$) and can be expressed as follows:

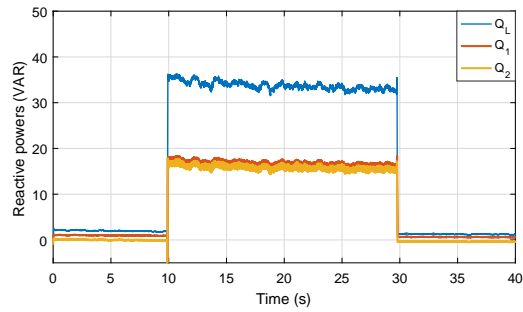
$$\begin{cases} V_1 = V_{Load} + \sqrt{r_1^2 + x_1^2} \frac{I_{Load}}{3} \\ V_2 = V_{Load} + \sqrt{r_2^2 + x_2^2} \frac{2I_{Load}}{3} \end{cases} \quad (44)$$

From Fig. 23 and although the test was performed for a purely resistive load, a reactive powers oscillation occurs during the connection and disconnection of the second VSI. Besides, active power control is not independent from the reactive power one, as a change of the active power set value at 5s and 25s, also causes a transient change in reactive power sharing. In fact, Low-voltage microgrid lines present resistive properties (neglected in the proposed control strategy), which can lead to a strong coupling between active and reactive experimental power outputs. Here and in order to compensate the uneven line voltage drop of the two VSIs, an adequate sizing of VSI₁ filter ($x_1=2x_2$) can enormously reduce the coupling oscillations.

It can be observed also from Fig. 24, that the voltage at PCC is well regulated, which clearly mean that the proposed VSG-based control strategy is able to synchronize the two VSIs without PLL. Note here that high-frequency oscillations can be observed in the output currents and voltages, despite the use of a first-order low pass filter for output currents and voltages measurement. This is due to a practical constraint related to the LC filters sizing, which has



(a)



(b)

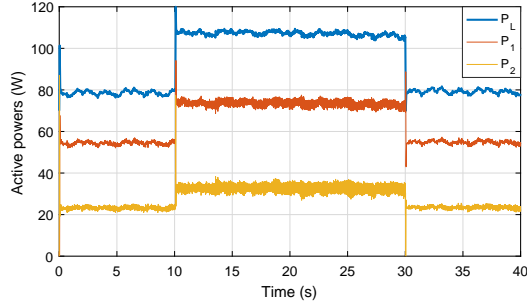
Figure 25: Experimental power sharing result for $R = 1$. a) Active power sharing, b) Reactive power sharing.

been carried out according to the laboratory available inductance and capacitor
 450 (Table 2).

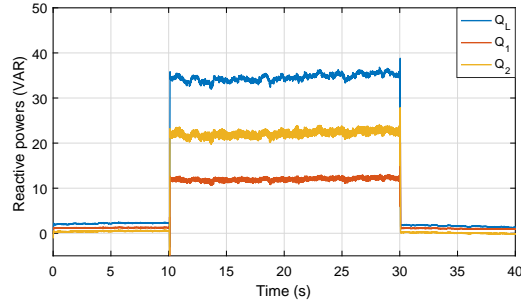
5.2. Power Sharing Method Experimental Validation

In this part, the two VSIs are connected in parallel in order to evaluate
 the practical feasibility of the proposed power sharing, according to the desired
 power ratio R . Initially, the system operates with the first load then the second
 455 load is connected at $t = 10s$ before cutting off from the system at $t = 30s$.

Figures 25 to 27, corresponds to a desired power ratio of $R = 1, 2, \text{ and } 3$,
 respectively. In each test, the waveforms from top to down are the load active
 power, VSI₁ output active power, VSI₂ output active power, load reactive power,



(a)



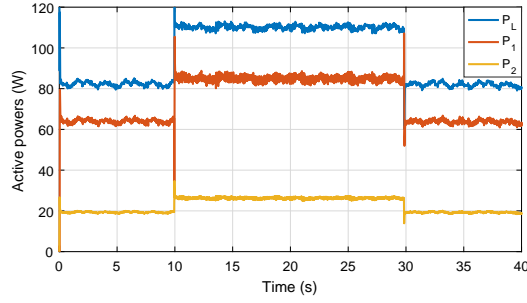
(b)

Figure 26: Experimental power sharing result for $R = 3$. a) Active power sharing, b) Reactive power sharing.

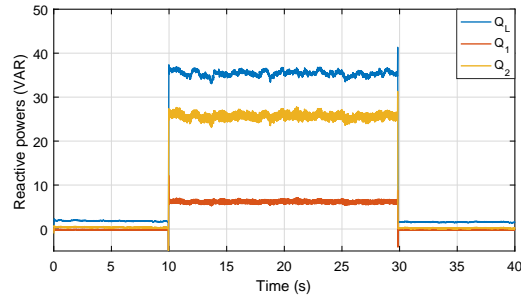
VSI_1 output reactive power, and VSI_2 output reactive power, respectively.

460 These achieved results clearly show that the two VSIs contribute to the load power demand by a set beforehand power ratio. Again, they validate the effectiveness of the proposed power sharing method. In fact, by applying the VSG control, the active and reactive powers are shared according to the desired power ratios of VSI_1 and VSI_2 .

465 In order to improve the system stability, the virtual inertia J and the damping coefficient D must be judiciously chosen. The system response is slow with a relatively large inertia and quick with a relatively small inertia. It is strongly emphasized that the practical value of the virtual inertia of VSI_1 ($J_1 = 0.22$, given in Table 2) has been chosen for a better system stability; while the prac-



(a)



(b)

Figure 27: Experimental power sharing result for $R = 3$. a) Active power sharing, b) Reactive power sharing.

470 tical value of the virtual inertia of VSI₂ ($J_2 = 0.06$, given in Table 2) has been chosen corresponding to the diesel generator parameters. While the damping coefficients ($D1_{R1} = D2$, $D1_{R2} = 2D2$, $D1_{R3} = 3D2$) have been adjusted according to the desired active power ratio R , as discussed in Subsection 3.2.3

6. Conclusion

475 In this paper, a new virtual synchronous generator-based control strategy has been proposed for a hybrid PV-Diesel power system in a stand-alone context. The control idea aims to synchronize the VSI and the DG without a PLL and with correction of the diesel generator rotor initial position. In the proposed approach, the active and reactive powers sharing between the two energy sources

480 can be envisaged with a desired ratio.

Simulations and experiments under load variation have successfully proved the effectiveness of the proposed virtual synchronous generator-based control strategy. It has been particularly demonstrated that the proposed control ensures synchronism and achieves powers sharing according to the desired power
485 ratio.

References

- [1] Y.-S. Kim, E.-S. Kim, S.-I. Moon, Frequency and voltage control strategy of standalone microgrids with high penetration of intermittent renewable generation systems, *IEEE Transactions on Power systems* 31 (1) (2016) 718–728.
490
- [2] A. Belila, M. Benbouzid, E.-M. Berkouk, Y. Amirat, On energy management control of a pv-diesel-ess based microgrid in a stand-alone context, *Energies* 11 (8) (2018) 2164.
- [3] T. E. Tawil, J. F. C. M. Benbouzid, G. Yao, Design, analysis, and comparison of inverter control methods for microgrid application for stand-alone sites, in: *2017 IEEE International Electrical Machines and Drives Conference*, 2017, pp. 1–6.
495
- [4] J. Alipoor, Y. Miura, T. Ise, Power system stabilization using virtual synchronous generator with alternating moment of inertia, *IEEE Journal of Emerging and Selected Topics in Power Electronics* 3 (2) (2015) 451–458.
500
- [5] L. Lu, C. Chu, Consensus-based secondary frequency and voltage droop control of virtual synchronous generators for isolated ac micro-grids, *IEEE Journal on Emerging and Selected Topics in Circuits and Systems* 5 (3) (2015) 443–455.
- [6] H. Bevrani, T. Ise, Y. Miura, Virtual synchronous generators: A survey and new perspectives, *International Journal of Electrical Power & Energy Systems* 54 (2014) 244–254.
505

- [7] B. Zhang, X. Yan, D. Li, X. Zhang, J. Han, X. Xiao, Stable operation and small-signal analysis of multiple parallel dg inverters based on a virtual synchronous generator scheme, *Energies* 11 (1) (2018). doi:10.3390/en11010203. 510
- [8] H. Zhao, Q. Yang, H. Zeng, Multi-loop virtual synchronous generator control of inverter-based dgs under microgrid dynamics, *IET Generation, Transmission Distribution* 11 (3) (2017) 795–803. doi:10.1049/iet-gtd.2016.0645. 515
- [9] T. E. Tawil, G. Yao, J. F. Charpentier, M. E. H. Benbouzid, Design and analysis of a virtual synchronous generator control strategy in microgrid application for stand-alone sites, *IET Generation, Transmission Distribution* x (x) (2019) 1–8.
- [10] W. Wu, Y. Chen, A. Luo, L. Zhou, X. Zhou, L. Yang, Y. Dong, J. M. Guerrero, A virtual inertia control strategy for dc microgrids analogized with virtual synchronous machines, *IEEE Transactions on Industrial Electronics* 64 (7) (2017) 6005–6016. 520
- [11] C. Gao, X. Liu, H. Chen, Research on the control strategy of distributed energy resources inverter based on improved virtual synchronous generator, Tech. rep., in *matworks models* (2017). 525
- [12] G. Yao, Z. Lu, M. Benbouzid, T. Tang, J. Han, A virtual synchronous generator based inverter control method for distributed generation systems, in: *IECON 2015 - 41st Annual Conference of the IEEE Industrial Electronics Society*, 2015, pp. 002112–002117. doi:10.1109/IECON.2015.7392413. 530
- [13] H. Xu, X. Zhang, F. Liu, R. Shi, C. Yu, R. Cao, A reactive power sharing strategy of vsg based on virtual capacitor algorithm, *IEEE Transactions on Industrial Electronics* 64 (9) (2017) 7520–7531.
- [14] B. Li, L. Zhou, Power decoupling method based on the diagonal compen-

- 535 sating matrix for vsg-controlled parallel inverters in the microgrid, *Energies* 10 (12) (2017) 2159.
- [15] Y. Han, H. Li, P. Shen, E. A. A. Coelho, J. M. Guerrero, Review of active and reactive power sharing strategies in hierarchical controlled microgrids, *IEEE Transactions on Power Electronics* 32 (3) (2017) 2427–2451.
- 540 [16] S. Y. Altahir, X. Yan, A. S. Gadalla, Active and reactive power sharing control strategy for vsGs in microgrid considering the different capacities of distributed energy resources, *IET Cyber-Physical Systems: Theory & Applications* 3 (3) (2018) 167–173.
- [17] J. Liu, Y. Miura, H. Bevrani, T. Ise, Enhanced virtual synchronous generator control for parallel inverters in microgrids, *IEEE Transactions on Smart Grid* 8 (5) (2017) 2268–2277.
- 545 [18] D. Chen, Y. Xu, A. Q. Huang, Integration of dc microgrids as virtual synchronous machines into the ac grid, *IEEE Transactions on Industrial Electronics* 64 (9) (2017) 7455–7466.
- 550 [19] J. Alipoor, Y. Miura, T. Ise, Stability assessment and optimization methods for microgrid with multiple vsg units, *IEEE Transactions on Smart Grid* 9 (2) (2018) 1462–1471. doi:10.1109/TSG.2016.2592508.
- [20] I. Serban, C. P. Ion, Microgrid control based on a grid-forming inverter operating as virtual synchronous generator with enhanced dynamic response capability, *International Journal of Electrical Power & Energy Systems* 89 (2017) 94–105.
- 555 [21] M. Datta, T. Senjyu, A. Yona, T. Funabashi, C. Kim, A frequency-control approach by photovoltaic generator in a pvdiesel hybrid power system, *IEEE Transactions on Energy Conversion* 26 (2) (2011) 559–571. doi:10.1109/TEC.2010.2089688.
- 560

- [22] M. Choopani, S. Hosseinain, B. Vahidi, A novel comprehensive method to enhance stability of multi-vsg grids, *International Journal of Electrical Power & Energy Systems* 104 (2019) 502–514.
- [23] Y. Hirase, K. Abe, K. Sugimoto, K. Sakimoto, H. Bevrani, T. Ise, A novel control approach for virtual synchronous generators to suppress frequency and voltage fluctuations in microgrids, *Applied Energy* 210 (2018) 699–710.
- [24] U. Bose, S. K. Chattopadhyay, C. Chakraborty, B. Pal, A novel method of frequency regulation in microgrid, *IEEE Transactions on Industry Applications* 55 (1) (2019) 111–121.
- [25] M. Farrokhbadi, C. A. Caizares, K. Bhattacharya, Frequency control in isolated/islanded microgrids through voltage regulation, *IEEE Transactions on Smart Grid* 8 (3) (2017) 1185–1194. doi:10.1109/TSG.2015.2479576.
- [26] A. Belila, B. Tabbache, A control strategy of hybrid system diesel-photovoltaic-battery for stand-alone applications, in: 2015 IEEE 15th International Conference on Environment and Electrical Engineering (EEEIC), 2015, pp. 860–865. doi:10.1109/EEEIC.2015.7165276.
- [27] A. Belila, B. Tabbache, E. Berkouk, M. Benbouzid, Integration of a storage system in a hybrid system "diesel-photovoltaic" for stand-alone applications, in: 2017 IEEE International Conference on Environment and Electrical Engineering and 2017 IEEE Industrial and Commercial Power Systems Europe (EEEIC / I CPS Europe), 2017, pp. 1–6. doi:10.1109/EEEIC.2017.7977884.
- [28] J. Rocabert, A. Luna, F. Blaabjerg, P. Rodriguez, Control of power converters in ac microgrids, *IEEE Transactions on Power Electronics* 27 (11) (2012) 4734–4749.
- [29] M. Chen, X. Xiao, Hierarchical frequency control strategy of hybrid

droop/vsg-based islanded microgrids, *Electric Power Systems Research* 155 (2018) 131–143.

590 [30] S. DArco, J. A. Suul, O. B. Fosso, A virtual synchronous machine implementation for distributed control of power converters in smartgrids, *Electric Power Systems Research* 122 (2015) 180–197.

[31] C. Gao, X. Liu, H. Chen, Research on the control strategy of distributed energy resources inverter based on improved virtual synchronous generator, *Scientific reports* 7 (1) (2017) 9025.
595

[32] Hou, Xiaochao and Sun, Yao and Zhang, Xin and Lu, Jinghang and Wang, Peng and Guerrero, Josep M, Improvement of Frequency Regulation in VSG-Based AC Microgrid via Adaptive Virtual Inertia, *IEEE Transactions on Power Electronics*, Early access (2019). doi:10.1109/TPEL.2019.2923734.
600

[33] H. G. C. Amodeo, Santiago J., A. R. Oliva., High-performance control of a dc-dc z-source converter used for an excitation field driver., *IEEE Trans.Power Electronics* 27 (6) (2012) 2947–2957.